Article

Enhanced Photocatalytic Degradation of Rhodamine B Dye by Iron-Doped Europium Oxide Nanoparticles

Xin Zhao,[⊥] Yishuai Jing,[⊥] Zhonghua Dai, Yuanbo Chu, Zhenyu Liu, Yu Cong, and Jiaming Song*

Cite This: *ACS Omega* 2024, 9, 16868−16875

Read Online

ACCESS		Metrics & More		Article Recommendations

ABSTRACT: As a wide-bandgap rare-earth oxide, Eu_2O_3 was often utilized as an auxiliary material of other photocatalysts because its photocatalytic performance was limited by the luminescence characteristics of Eu^{3+} and low light utilization. In this study, we improved the photocatalytic degradation performance of the Eu_2O_3 nanoparticles by doping with Fe cations. The Eu_2O_3 nanoparticles with different Fe-doping concentrations (1, 3, and 5%, noted as EF1.0, EF3.0, and EF5.0, respectively) were synthesized via chemical precipitation and calcination methods. It was found that doping could reduce Eu_2O_3's bandgap, which probably originated from the introduction of oxygen vacancies with lower energy levels than the conduction band of Eu_2O_3. Compared with the undoped Eu_2O_3 nanoparticles with a removal efficiency of 22% for degrading rhodamine B dye within 60 min, the photocatalytic degradation efficiencies of EF1.0, EF3.0, and EF5.0 were demonstrated to be improved to 42, 48, and 33%, respectively, and EF3.0's performance was the best. The enhanced photocatalytic performance of the doped samples was related to the oxygen vacancies acting as capture centers for electrons, such that the photogenerated electron−hole pairs were efficiently separated and the redox reactions on the surface of the nanoparticles were enhanced accordingly. Additionally, the enhanced light absorption and broadened spectral band further improved EF3.0's degradation efficiency.
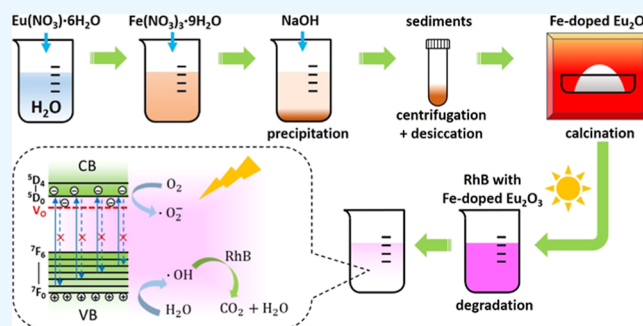
1. INTRODUCTION

The treatment of organic wastewater from factories and organic chemicals used in agricultural production processes is one of the major challenges in pollution control of the environment.[1−3] In recent years, photocatalytic technology based on semiconducting oxides has been utilized for degradation of various organic pollutants owing to their high efficiency, environmental friendliness, and high oxidation capacity.[4,5] Up to now, many oxide photocatalysts have been excavated, such as TiO_2,[5−7] ZnO,[8−10] SnO_2,[11−13] Ga_2O_3,[14−16] WO_3,[4,17,18] perovskites,[19,20] etc. The degradation mechanism of photocatalysis depends on the formation of electron−hole pairs in a photocatalyst by light irradiation. When the photocatalyst is irradiated by light with energy higher than its bandgap, electrons will be excited to the conduction band (CB), leaving holes in the valence band (VB). Subsequently, the photogenerated electrons and holes will transfer to the surface of the photocatalyst and produce reactive oxygen species, such as superoxide anions ($\bullet O_2^-$) and hydroxyl radicals ($\bullet OH$).[14] These reactive oxygen species with strong redox ability will react with organic pollutants and degrade them into smaller, nontoxic molecules.[14,15,21] Therefore, improving the electron−hole separation efficiency is critical to the photocatalytic process.

In general, wide-bandgap semiconductors have greater catalytic capacity compared with narrow-bandgap ones due to the higher oxidation potential of holes or reduction potential of electrons.[22] However, the ultraviolet absorption band of the wide-bandgap semiconductors mainly absorbs ultraviolet light, which takes only 5−7% proportion of solar light, limiting the utilization rate of the solar light and the photocatalysts' degradation ability. Among these wide-bandgap semiconductors, rare-earth oxide Eu_2O_3 exhibited potential capacity in photocatalytic applications.[23−25] Nevertheless, due to europium's unique 4f electron shell with split energy levels, the electric dipole transition could lead to photogenerated charge carrier recombination that is not favored in the photocatalytic degradation process.[26,27] Besides, the low light utilization caused by the wide bandgap of Eu_2O_3[28] restrained its photocatalytic capacity. Up to now, most Eu_2O_3 and europium cations-related photocatalytic studies are mainly
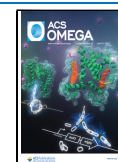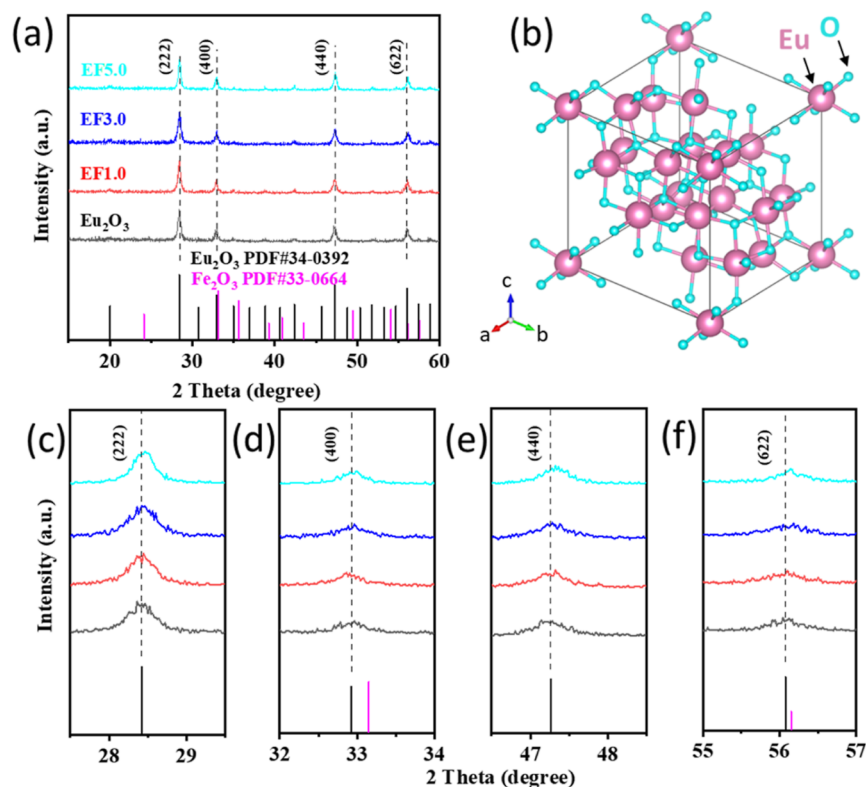
Figure 1. (a) XRD patterns of Eu_2O_3, EF1.0, EF3.0, and EF5.0. (b) Structure model of a body-centered cubic Eu_2O_3 unit cell. (c–f) XRD peaks from (a) displayed in different diffraction angle ranges.

about their auxiliary effect for enhancing other materials' photocatalytic performances.[29−33] For Eu_2O_3 itself as a photocatalyst, how to improve the material's photocatalytic degradation efficiency is an interesting topic to be explored. There are several ways for improving a photocatalyst's degradation capacity, such as to increase the active reaction sites, to enhance the light absorption, to inhibit/enhance the recombination/separation of photogenerated electrons and holes, and so forth. Practically, doping is a commonly used method for improving the charge carrier separation efficiency and light absorption in semiconductors. Metal ion doping, like Sr^{2+} in SnO_2,[21] Zn^{2+} in Ga_2O_3 nanofibers,[34] and the others,[26,35,36] could introduce defects like oxygen vacancies with energy levels located within the bandgap of the oxides, and these oxygen vacancies acted as trapping states for electrons, such that the recombination of the photogenerated carriers was inhibited. Moreover, the bandgap of the material could be reduced, and thus, the light absorption band could be broader to enable a higher utilization efficiency of the light. Thereby, to harness the method of foreign element doping in Eu_2O_3 could be a promising way for promoting the material's photocatalytic performance.

In this work, we investigated the photocatalytic degradation performance of Fe-doped Eu_2O_3 nanoparticles synthesized by chemical precipitation and calcination methods. The crystalline structure, morphology, surface chemical states, and light absorption capacity, as well as the photoluminescence (PL) properties, were characterized and analyzed. Different molar ratios of Fe-doped Eu_2O_3 were prepared, and their photo-catalytic degradation efficiencies for degrading organic rhod-amine B (RhB) dye were compared. The possible mechanism of the improved photocatalytic degradation performance was

analyzed. This study demonstrates a possible route for improving the rare-earth oxide Eu_2O_3's photocatalytic degradation ability and confirms its potential application value in terms of environmental governance.

2. RESULTS AND DISCUSSION

The crystalline structures of the undoped Eu_2O_3 and Fe-doped Eu_2O_3 nanoparticles were characterized by X-ray diffraction (XRD), as shown in Figure 1. It is seen in Figure 1a that all of the observed peaks can be well indexed to the body-centered cubic phase of Eu_2O_3 (PDF#34-0392). The lattice parameters are $a = b = c = 1.087$ nm and $\alpha = \beta = \gamma = 90°$, and the space group belongs to $Ia\bar{3}$ (206), as the structural model shows in Figure 1b. There is no other peak observed for the Fe-doped nanoparticles, indicating that Fe did not form any other compounds but only acted as dopants.[38] The peaks at 28.42, 32.93, 47.27, and 56.08° correspond to the (222), (400), (440), and (622) lattice planes, respectively. In Figure 1c−f, it is seen that all these diffraction peaks demonstrate gradual slight shifts toward higher angles with the increase of the doping concentration, which could be possibly due to the shrinkage of lattice distances caused by the smaller radii of Fe^{3+} cations incorporated in the Eu_2O_3 lattice, suggesting that Fe cations were successfully doped into the lattice of Eu_2O_3. We also calculated the average crystallite sizes of the nanoparticles according to the Debye−Scherrer equation: $D = K\lambda/(B \cos \theta)$, where D is the average thickness of the grain in the direction perpendicular to the lattice plane, B is the full width at half maxima of the measured diffraction peak, K is the Scherrer constant which equals 0.89, θ is the Bragg diffraction angle, and $\lambda = 0.15406$ nm is the wavelength of the X-ray from the Cu $K\alpha$ radiation source. Lower-angle diffraction peaks for the

(222) and (400) lattice planes were used for the calculation. The obtained average crystallite sizes for Eu_2O_3, EF1.0, EF3.0, and EF5.0 are 20.56, 24.84, 24.95, and 29.62 nm, respectively, indicating that the crystallite size of the doped nanoparticles increases with the Fe-doping concentration. Besides, the surface morphologies of the doped and undoped Eu_2O_3 nanoparticles were characterized by scanning electron microscopy (SEM), as shown in Figure 2. It can be observed
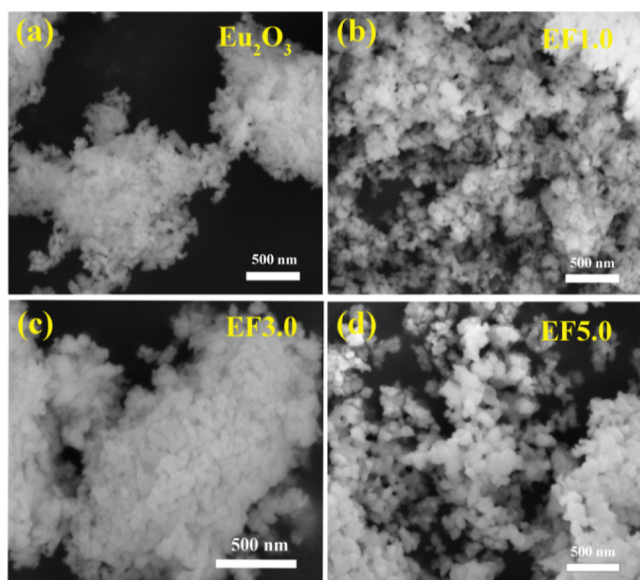

Figure 2. SEM images of undoped Eu_2O_3 (a), EF1.0 (b), EF3.0 (c), and EF5.0 (d).

that these nanoparticles exhibit different degrees of agglomeration. As the doping concentration increased, the agglomer-

ation became more and more significant, which could be due to the slight variation of pHs during the precipitation procedure.[37]

To further analyze the surface chemical states of the nanoparticles and identify the existence of Fe cations, we performed the X-ray photoelectron spectroscopy (XPS) measurement, as shown in Figure 3. The full spectra for Eu_2O_3 and Fe-doped Eu_2O_3 in Figure 3a show that there was no obvious peak for the Fe element except for those of the Eu and O elements. The possible reason could be attributed to the weak signal of Fe compared to that of the others. A clear display of peaks for the Fe 2p orbitals is shown in Figure 3b. The peaks at 710.35 and 710.03 eV correspond to the Fe $2p_{3/2}$ orbitals of EF3.0 and EF5.0, respectively, indicating the presence of Fe^{3+} in the Eu_2O_3 lattice.[3] Due to the low percentage of Fe in EF1.0, the peak near 710.00 eV was not significant. In Figure 3c, two groups of peaks located near 1150 eV are attributed to large spin−orbit interactions of the Eu 3d electrons. The group of peaks lower than 1150 eV is associated with Eu $3d_{5/2}$ electronic states, and the higher ones are for Eu $3d_{3/2}$ states. Here, the peaks labeled with * and # correspond to Eu^{3+} and Eu^{2+} ions, respectively.[30,38] The small amount of Eu^{2+} could possibly originate from the "surface-valence-transition" phenomenon of the surface layer, which was discovered in many rare-earth compounds before.[38−40] Besides, the small peaks labeled as "mult" near 1145 eV are consistent with the theoretical calculation by using the multiplet structure of 3d4f.[6,39] The peaks near 1170 eV for the Fe-doped nanoparticles could be attributed to the similar origin as the "mult" ones. The electronic states of the O 1s were split into three peaks marked as O_i, O_{ii}, and O_{iii}, respectively, as shown in Figure 3d. As the Fe-doping concentration increases, the peaks for the surface lattice oxygen (O_i) and oxygen in the Eu−O bonds (O_{ii}) both tend to
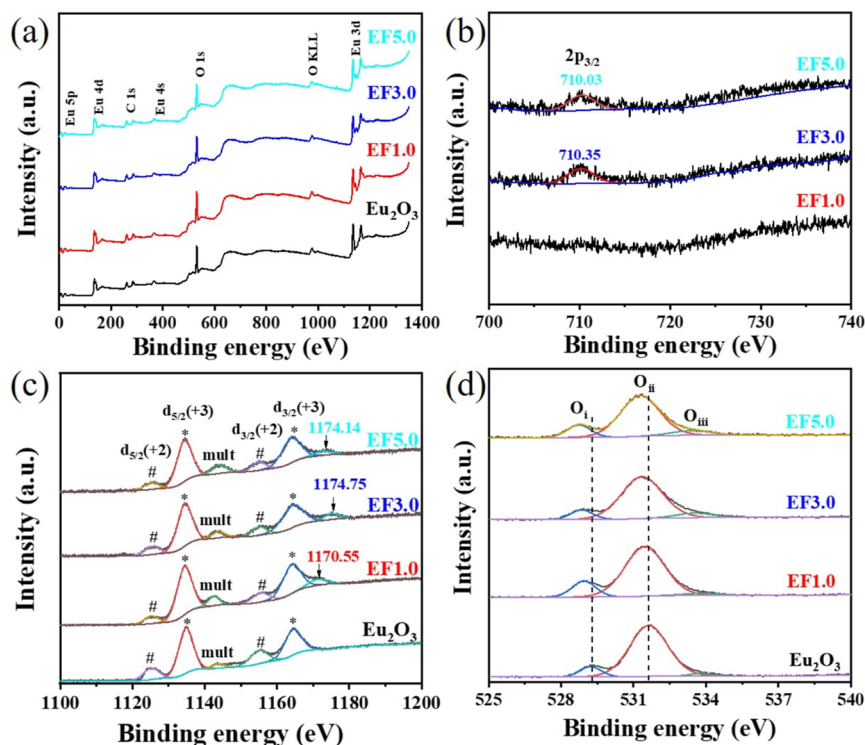

Figure 3. XPS survey spectra (a) and the fine spectra of Fe 2p (b), Eu 3d (c), and O 1s (d) orbitals.
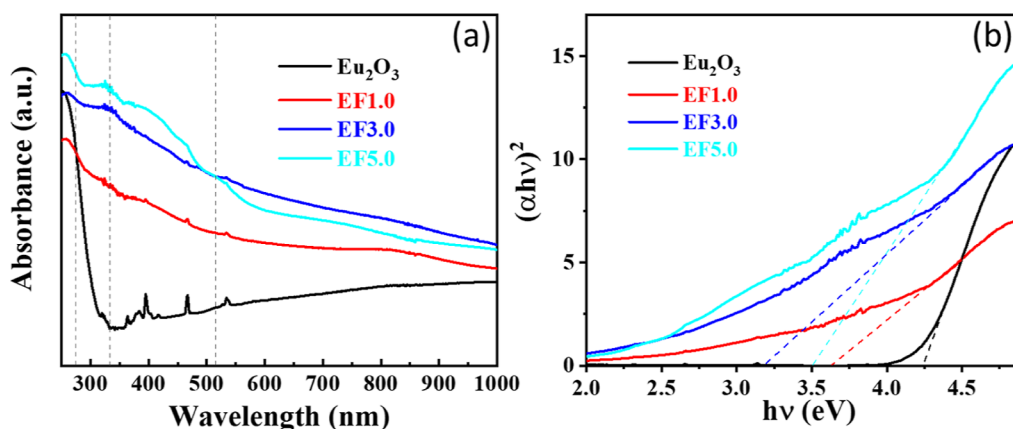
Figure 4. UV−vis DRS spectra (a) and the corresponding Tauc plots between 275 and 620 nm (b) for Eu_2O_3, EF1.0, EF3.0, and EF5.0.
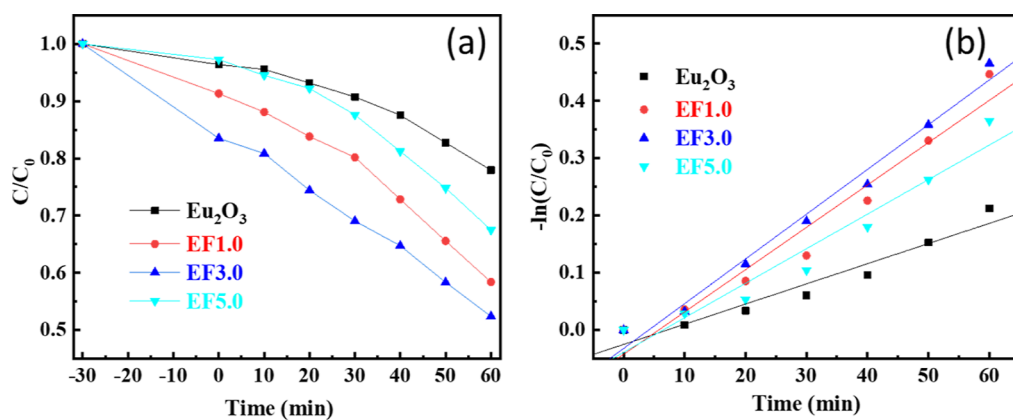

Figure 5. (a) Removal efficiency curves and (b) photocatalytic degradation rate curves for Eu_2O_3, EF1.0, EF3.0, and EF5.0 under Xe lamp irradiation.

shift to lower binding energies. The O_{iii} peaks are attributed to the existence of surface chemically adsorbed oxygen, such as oxygen in hydroxyl groups, etc.[41]

The light absorption spectra of the Eu_2O_3-based nanoparticles are shown in Figure 4a. It is seen that Eu_2O_3 demonstrates a strong absorption range between 250 and 333 nm. For the light wavelengths between 275 and 500 nm, the overall absorption intensities of EF1.0, EF3.0, and EF5.0 tend to have a positive correlation with the Fe-doping concentration. However, EF3.0 demonstrates to have a broader absorption band than others and exhibits the strongest absorption above 515 nm. To analyze the optical bandgap change caused by the Fe-doping effect, the corresponding Tauc plots of the absorption spectra in Figure 4a are shown in Figure 4b by using the following equation

$$(\alpha h\nu)^2 = A(h\nu - E_g) \tag{1}$$

where A is a constant, α is the absorption coefficient, and E_g is the optical bandgap of the material. In Figure 4b, the extended dotted line for the linear section of each absorption curve intersects with the abscissa axis, giving rise to the E_g value at the intersection point. The obtained bandgaps of Eu_2O_3, EF1.0, EF3.0, and EF5.0 are 4.23, 3.64, 3.18, and 3.50 eV, respectively. It is seen that the optical bandgaps of EF1.0, EF3.0, and EF5.0 are distinctly reduced compared with that of Eu_2O_3, which could be probably due to the introduced O vacancies by the doping of Fe^{3+}.

The photocatalytic degradation capacities of these doped and undoped Eu_2O_3 nanoparticles were examined by using RhB as a colored organic dye, as presented in Figure 5. The removal efficiency curves in Figure 5a illustrate the relative concentration of the RhB solution (C/C_0) versus the irradiation time. According to the Lambert−Beer law,[14] C_0 and C correspond to the absorbance intensities of RhB solution in the UV−vis absorbance spectra at 554 nm. These removal efficiency curves show that, compared with the undoped Eu_2O_3 particles with a removal efficiency of 22% within 60 min, all Fe-doped nanoparticles demonstrated significantly enhanced efficiencies of 42, 48, and 33% for EF1.0, EF3.0, and EF5.0, respectively. In order to further analyze the photocatalytic degradation of RhB, we fit the data points obtained from the photocatalytic process, as illustrated in Figure 5b. The fittings followed the Langmuir−Hinshelwood pseudo-first-order kinetic model, as illustrated as follows

$$-\ln(C/C_0) = kt \tag{2}$$

where k and t are the pseudo-first-order constant and irradiation time, respectively. The slopes of these linear fittings correspond to the degradation rates of the photocatalysts. According to Figure 5b, the obtained k values for Eu_2O_3, EF1.0, EF3.0, and EF5.0 are 0.0035, 0.0074, 0.0078, and 0.0061 min^{-1}, respectively. It is known that all the Fe^{3+}-doped nanoparticles have superior photocatalytic degradation performance compared to that of Eu_2O_3, and EF3.0 demonstrates the highest photocatalytic degradation rate, which proves that

the doping of Fe^{3+} in Eu_2O_3 can effectively improve the photocatalytic performance of the catalysts. In Table 1, we

Table 1. Photocatalytic Removal Efficiencies of Rare-Earth Oxides in Degradation of RhB

photocatalyst	photocatalyst concentration (g/L)	RhB concentration	xenon lamp power (W)	removal efficiency with 1 h (%)
Y_2O_3[42]	0.4	4 mg/L	300	25
La_2O_3[43]	1	10 mg/L	300	19
CeO_2[44]	1	1×10^{-5} mol/L	300	20
CeO_2[45]	1	1×10^{-5} mol/L	500	10
Eu_2O_3/Ag[46]	0.5	10 mg/L	50	20
Eu_2O_3 (this work)	1	10 mg/L	500	22
EF3.0 (this work)	1	10 mg/L	500	48

compared the photocatalytic degradation efficiencies of EF3.0 and other rare-earth oxides for RhB removal. It is seen that EF3.0 demonstrates a competitive photocatalytic degradation performance among these rare-earth oxides.

In order to interpret the possible scenario for the enhanced photocatalytic degradation ability of the Eu_2O_3 nanoparticles by Fe^{3+} doping, we performed PL measurements of the photocatalysts, as shown in Figure 6. According to the excitation spectra (Figure 6a) and the ultraviolet–visible diffuse reflectance spectroscopy (UV–vis DRS) results (Figure 4), the PL spectra were measured at two different excitation wavelengths of 280 and 467 nm, respectively, as shown in

Figure 6b,c. In both Figure 6b,c, five groups of characteristic peaks are observed between 550 and 750 nm, ascribed to the $^5D_0 \rightarrow {}^7F_J$ (J = 0, 1, 2, 3, and 4) of the Eu^{3+} 4f–4f transition.[26] It is observed that peaks corresponding to the electric dipole transition ($^5D_0 \rightarrow {}^7F_2$) are much stronger than those for other transitions, indicating that the Eu^{3+} hosts occupied low-symmetry sites without inversion centers.[47] Besides, the $^5D_0 \rightarrow {}^7F_1$, $^7F_2$, and $^7F_4$ transitions all split into different peaks due to the energy level splitting originated from different Eu^{3+}-site occupations.[27,47] In contrast to Eu_2O_3, the doped nanoparticles exhibited a distinct decrease of the peak intensities, and those for both EF3.0 and EF5.0 demonstrated to be even lower than that of EF1.0, indicating that photogenerated carrier recombination in EF3.0 and EF5.0 was relatively less and Fe doping significantly inhibited the recombination process. One possible scenario could be due to the oxygen vacancies introduced by the doping of Fe^{3+} cations, which act as trapping centers for photogenerated electrons, increasing the lifetime of photogenerated carriers. Here, the lowest PL peak intensities of EF3.0 coincide with its highest degradation rate, as shown in Figure 5b. Moreover, in both Figure 6b,c, it is found that with the increase of the Fe-doping concentration, peaks corresponding to each single transition gradually disappeared. This could be due to the fact that the doping of Fe^{3+} affected the symmetry of Eu^{3+} in the lattice. Accordingly, it is concluded that Fe-doped Eu_2O_3 particles have a lower electron–hole recombination rate and a higher charge separation efficiency in both UV and visible bands under 500 W Xe lamp irradiation. Despite the fact that the decrease in the bandgap (Figure 4b) of Fe-doped Eu_2O_3 could weaken the photocatalyst's redox
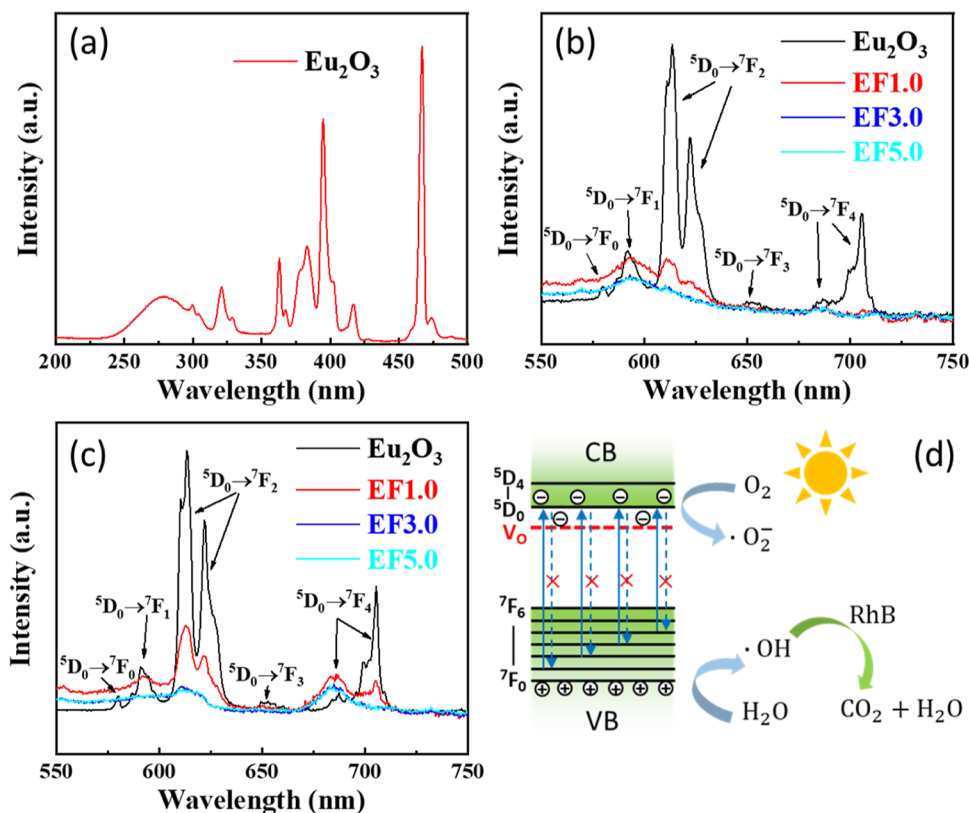

Figure 6. (a) Excitation spectrum of Eu_2O_3 nanoparticles. (b, c) PL spectra of Eu_2O_3, EF1.0, EF3.0, and EF5.0 at the excitation wavelengths of 280 and 467 nm, respectively. (d) Schematics of redox reactions on the energy bands of Fe-doped Eu_2O_3 nanoparticles. V_O represents the energy level (red dashed line) for the oxygen vacancies.

ability, the longer lifetime of photogenerated carriers and the increased light absorption together improved the photocatalytic degradation efficiency of the Fe-doped nanoparticles.

Figure 6d shows the redox reaction mechanism of Fe-doped Eu_2O_3 nanoparticles during the photocatalytic degradation process. Upon light irradiation, electrons in the VB of Eu_2O_3 were excited and transferred to the CB, forming electron–hole pairs. During this process, some photogenerated electrons in the CB could be trapped at these oxygen vacancies with lower energy levels near the CB, and the recombination from $^5D_0$ to $^7F_1$, $^7F_2$, $^7F_3$, or $^7F_4$ was partially inhibited, leading to enhanced separation of electron–hole pairs. Here, the low-concentration doping of Fe^{3+} in Eu_2O_3 could increase the concentration of oxygen vacancies, which facilitated achieving a higher separation efficiency of electron–hole pairs compared with that of undoped Eu_2O_3. Among all Fe-doped samples, EF3.0 has the smallest bandgap (3.18 eV), which means that there are probably more oxygen vacancies present and a wider visible light absorption band for EF3.0, giving rise to the best photocatalytic performance of EF3.0. Besides, the increase of Fe doping in EF5.0 did not improve the photocatalytic degradation of RhB further, which could be because more Fe^{3+} cations did not help add more oxygen vacancies and the energy bandgap was not further narrowed for a broader spectral absorption band.

3. CONCLUSIONS

In summary, the photocatalytic degradation performance of pure and Fe-doped Eu_2O_3 nanoparticles was investigated by utilizing RhB as the organic pollutant. The nanoparticles were synthesized by chemical precipitation and calcination methods. It was found that the doping of Fe cations in Eu_2O_3 nanoparticles could lead to a shrinkage of the material's optical bandgap and increase the light absorption, which could be possibly due to the introduction of oxygen vacancies by Fe doping. Photocatalytic degradation measurements demonstrated that all Fe-doped Eu_2O_3 showed enhanced photocatalytic performance, which was attributed to the improved separation efficiency of carriers by the oxygen vacancies, as confirmed by the PL spectra. Compared with other Fe-doped nanoparticles, the EF3.0 sample demonstrated the highest photocatalytic degradation efficiency of 48% for degrading RhB. This work provides a new sight for rare-earth oxides applied in highly efficient photocatalytic degradations and environmental pollution controls.

4. EXPERIMENTAL SECTION

4.1. Materials. Europium nitrate hexahydrate [$Eu(NO_3)_3 \cdot 6H_2O$, 99.99%] was sourced from Aladdin. Sodium hydroxide (NaOH, 96%) was purchased from the Hongyan Chemical Reagent Factory. Iron nitrate nonahydrate [$Fe(NO_3)_3 \cdot 9H_2O$, 98.5%] was supplied by the Damao Chemical Reagent Factory.

4.2. Synthesis. To prepare the Fe-doped Eu_2O_3 nanoparticles, we first dissolved three portions of 0.001 mol $Eu(NO_3) \cdot 6H_2O$ in three beakers with 40 mL of deionized water each and stirred for 10 min. Then, three different amounts of $Fe(NO_3)_3 \cdot 9H_2O$ were added with the calculated doping molar ratios ($Fe^{3+}:Eu^{3+}$) of 1, 3, and 5% into the solutions, respectively, and stirred for 5 min. Subsequently, three portions of 5 mL of NaOH (0.6 M) were slowly added into the beakers separately and stirred for 30 min to obtain the precipitated sediments. Next, these suspensions were centri-

fuged and washed with deionized water 4 times each and then dried at 80 °C for 12 h. Finally, Fe-doped Eu_2O_3 nanoparticles were achieved through a calcination process by heating the products at 700 °C for 3 h. The corresponding samples are labeled as EF1.0, EF3.0, and EF5.0 for the 1, 3, and 5% doping of Fe, respectively.

For the synthesis of the undoped Eu_2O_3 nanoparticles, the procedures were the same as the doped ones, except for avoiding adding the Fe source, i.e., $Fe(NO_3)_3 \cdot 9H_2O$.

4.3. Characterizations. The crystal structure was characterized by an X-ray powder diffractometer (DX-2700, Hao Yuan, China) equipped with a Cu Kα radiation source (λ = 1.5406 Å). The morphology and particle size were characterized by SEM (FEI Apreo S). XPS (Thermo Scientific, EscaLab Xi+) was used to analyze the chemical state of elements via an Al Kα X-ray as the excitation source. The light absorption was measured by UV–vis DRS (F-7000 Hitachi, Japan). The PL spectrum was obtained via a fluorescence spectrometer (Edinburgh FLS920) equipped with a Xe lamp as the excitation light source.

4.4. Photocatalytic Degradation Tests. We tested the photocatalytic performances of EF1.0, EF3.0, and EF5.0 and the undoped Eu_2O_3 nanoparticles separately by using RhB as the organic pollutant. First, 50 mg of the photocatalyst was dispersed in 50 mL of RhB aqueous solution (10 mg/L) in a beaker. Before light irradiation, the beaker was kept in the dark, and the mixture was magnetically stirred for 30 min to reach an adsorption–desorption equilibrium of the dye on the surfaces of the nanoparticles. Then, the mixture inside the beaker was stirred continuously and irradiated under a 500 W Xe lamp for 60 min to enable the degradation reactions. During the irradiation process, 4 mL of the mixture was extracted from the beaker in every 10 min time interval and centrifuged at 9000 rpm for 20 min to completely remove the photocatalyst. Afterward, the absorption spectra of the obtained supernatant were measured by the UV–vis spectrophotometer.

■ AUTHOR INFORMATION

Corresponding Author

    Jiaming Song — *School of Physics, Northwest University, Xi'an 710127, China;* ◉ orcid.org/0000-0002-1931-1699; Email: jiaming.song@nwu.edu.cn

Authors

    Xin Zhao — *School of Optoelectronic Engineering, Xi'an Technological University, Xi'an 710021, China*

    Yishuai Jing — *School of Physics, Northwest University, Xi'an 710127, China*

    Zhonghua Dai — *School of Optoelectronic Engineering, Xi'an Technological University, Xi'an 710021, China*

    Yuanbo Chu — *School of Optoelectronic Engineering, Xi'an Technological University, Xi'an 710021, China*

    Zhenyu Liu — *College of Agricultural Engineering, Shanxi Agricultural University, Jinzhong 030801, China*

    Yu Cong — *Université Paris-Saclay, Univ Evry, LMEE, Evry 91020, France*

Complete contact information is available at:
https://pubs.acs.org/10.1021/acsomega.4c02280

Author Contributions

[⊥]X.Z. and Y.J. contributed equally.

Notes

The authors declare no competing financial interest.

REFERENCES

(1) Wang, H.; Zhang, L.; Chen, Z.; Hu, J.; Li, S.; Wang, Z.; Liu, J.; Wang, X. Semiconductor Heterojunction Photocatalysts: Design, Construction, and Photocatalytic Performances. *Chem. Soc. Rev.* **2014**, *43* (15), 5234−5244.

(2) Rueda-Marquez, J. J.; Levchuk, I.; Fernández Ibañez, P.; Sillanpää, M. A Critical Review on Application of Photocatalysis for Toxicity Reduction of Real Wastewaters. *J. Cleaner Prod.* **2020**, *258*, 120694.

(3) An, W.; Wang, H.; Yang, T.; Xu, J.; Wang, Y.; Liu, D.; Hu, J.; Cui, W.; Liang, Y. Enriched Photocatalysis-Fenton Synergistic Degradation of Organic Pollutants and Coking Wastewater via Surface Oxygen Vacancies over Fe-BiOBr Composites. *Chem. Eng. J.* **2023**, *451*, 138653.

(4) Szilágyi, I. M.; Fórizs, B.; Rosseler, O.; Szegedi, A.·.; Németh, P.; Király, P.; Tárkányi, G.; Vajna, B.; Varga-Josepovits, K.; László, K.; Tóth, A. L.; Baranyai, P.; Leskelä, M. WO₃ Photocatalysts: Influence of Structure and Composition. *J. Catal.* **2012**, *294*, 119−127.

(5) Qi, K.; Cheng, B.; Yu, J.; Ho, W. A Review on TiO₂-Based Z-Scheme Photocatalysts. *Chin. J. Catal.* **2017**, *38* (12), 1936−1955.

(6) Qi, K.; Liu, S.; Qiu, M. Photocatalytic Performance of TiO₂ Nanocrystals with/without Oxygen Defects. *Chin. J. Catal.* **2018**, *39* (4), 867−875.

(7) Guo, Q.; Zhou, C.; Ma, Z.; Yang, X. Fundamentals of TiO₂ Photocatalysis: Concepts, Mechanisms, and Challenges. *Adv. Mater.* **2019**, *31* (50), 1901997.

(8) Alam, U.; Khan, A.; Raza, W.; Khan, A.; Bahnemann, D.; Muneer, M. Highly Efficient Y and V Co-Doped ZnO Photocatalyst with Enhanced Dye Sensitized Visible Light Photocatalytic Activity. *Catal. Today* **2017**, *284*, 169−178.

(9) Koppala, S.; Xia, Y.; Zhang, L.; Peng, J.; Chen, Z.; Xu, L. Hierarchical ZnO/Ag Nanocomposites for Plasmon-Enhanced Visible-Light Photocatalytic Performance. *Ceram. Int.* **2019**, *45* (12), 15116−15121.

(10) Qi, K.; Xing, X.; Zada, A.; Li, M.; Wang, Q.; Liu, S.; Lin, H.; Wang, G. Transition Metal Doped ZnO Nanoparticles with Enhanced Photocatalytic and Antibacterial Performances: Experimental and DFT Studies. *Ceram. Int.* **2020**, *46* (2), 1494−1502.

(11) Wu, S.; Cao, H.; Yin, S.; Liu, X.; Zhang, X. Amino Acid-Assisted Hydrothermal Synthesis and Photocatalysis of SnO₂ Nanocrystals. *J. Phys. Chem. C* **2009**, *113* (41), 17893−17898.

(12) Huang, H.; Tian, S.; Xu, J.; Xie, Z.; Zeng, D.; Chen, D.; Shen, G. Needle-like Zn-Doped SnO₂ Nanorods with Enhanced Photocatalytic and Gas Sensing Properties. *Nanotechnology* **2012**, *23* (10), 105502.

(13) Peng, L.; Xiao, Y.; Wang, X.; Feng, D.; Yu, H.; Dong, X. Realization of Visible Light Photocatalysis by Wide Band Gap Pure SnO₂ and Study of In₂O₃ Sensitization Porous SnO₂ Photolysis Catalyst. *ChemistrySelect* **2019**, *4* (29), 8460−8469.

(14) Du, F.; Yang, D.; Kang, T.; Ren, Y.; Hu, P.; Song, J.; Teng, F.; Fan, H. SiO₂/Ga₂O₃ Nanocomposite for Highly Efficient Selective Removal of Cationic Organic Pollutant via Synergistic Electrostatic Adsorption and Photocatalysis. *Sep. Purif. Technol.* **2022**, *29S*, 121221.

(15) Kang, T.; Yang, D.; Du, F.; Hu, P.; Teng, F.; Fan, H. Using Magnesium Reduction Strategy to Produce Black Ga₂O₃ with Variable Oxygen Vacancies for Photocatalytic Applications. *J. Alloys Compd.* **2022**, *926*, 166887.

(16) Michel, C. R.; Martínez-Preciado, A. H. Photocatalytic Performance of β-Ga₂O₃ Microcubes towards Efficient Degradation of Malachite Green. *Ceram. Int.* **2022**, *48* (7), 9746−9752.

(17) Tahir, M. B.; Nabi, G.; Rafique, M.; Khalid, N. R. Nanostructured-Based WO₃ Photocatalysts: Recent Development, Activity Enhancement, Perspectives and Applications for Wastewater Treatment. *Int. J. Environ. Sci. Technol.* **2017**, *14* (11), 2519−2542.

(18) Liao, M.; Su, L.; Deng, Y.; Xiong, S.; Tang, R.; Wu, Z.; Ding, C.; Yang, L.; Gong, D. Strategies to Improve WO₃-Based Photocatalysts for Wastewater Treatment: A Review. *J. Mater. Sci.* **2021**, *56* (26), 14416−14447.

(19) Schanze, K. S.; Kamat, P. V.; Yang, P.; Bisquert, J. Progress in Perovskite Photocatalysis. *ACS Energy Lett.* **2020**, *5* (8), 2602−2604.

(20) Dandia, A.; Saini, P.; Sharma, R.; Parewa, V. Visible Light Driven Perovskite-Based Photocatalysts: A New Candidate for Green Organic Synthesis by Photochemical Protocol. *Curr. Res. Green Sustainable Chem.* **2020**, *3*, 100031.

(21) Ahmed, A.; Naseem Siddique, M.; Alam, U.; Ali, T.; Tripathi, P. Improved Photocatalytic Activity of Sr Doped SnO₂ Nanoparticles: A Role of Oxygen Vacancy. *Appl. Surf. Sci.* **2019**, *463*, 976−985.

(22) Fujishima, A.; Rao, T. N.; Tryk, D. A. Titanium Dioxide Photocatalysis. *J. Photochem. Photobiol., C* **2000**, *1* (1), 1−21.

(23) Gillen, R.; Clark, S. J.; Robertson, J. Nature of the Electronic Band Gap in Lanthanide Oxides. *Phys. Rev. B: Condens. Matter Mater. Phys.* **2013**, *87* (12), 125116.

(24) Gao, M.; Yan, C.; Li, B. Z.; Zhou, L. J.; Yao, J. C.; Zhang, Y. J.; Liu, H. L.; Cao, L. H.; Cao, Y. T.; Yang, J. H.; Wang, Y. X. Strong Red Emission and Catalytic Properties of ZnO by Adding Eu₂O₃ Shell. *J. Alloys Compd.* **2017**, *724*, 537−542.

(25) Jing, Y.; Kang, T.; Hu, P.; Fan, H.; Teng, F.; Zhao, X.; Song, J. Surfactant-Induced Photocatalytic Performance Enhancement of Europium Oxide Nanoparticles. *Process Saf. Environ. Prot.* **2023**, *171*, 888−894.

(26) Stojadinović, S.; Radić, N.; Grbić, B.; Maletić, S.; Stefanov, P.; Pačevski, A.; Vasilić, R. Structural, Photoluminescent and Photocatalytic Properties of TiO₂:Eu³⁺ Coatings Formed by Plasma Electrolytic Oxidation. *Appl. Surf. Sci.* **2016**, *370*, 218−228.

(27) Ding, K.; Siru, A.; Pang, S.; Shan, L.; Zhang, Y.; Sun, P.; Deng, B.; Yu, R. A Potential Red-Emitting Phosphor Ca₂YTaO₆:Eu³⁺: Luminescence Properties, Thermal Stability and Applications for White LEDs. *J. Rare Earths* **2021**, *39* (7), 749−756.

(28) Kumar, S.; Prakash, R.; Choudhary, R. J.; Phase, D. M. Structural, XPS and Magnetic Studies of Pulsed Laser Deposited Fe Doped Eu₂O₃ Thin Film. *Mater. Res. Bull.* **2015**, *70*, 392−396.

(29) Sin, J.-C.; Lam, S.-M.; Satoshi, I.; Lee, K.-T.; Mohamed, A. R. Sunlight Photocatalytic Activity Enhancement and Mechanism of Novel Europium-Doped ZnO Hierarchical Micro/Nanospheres for Degradation of Phenol. *Appl. Catal., B* **2014**, *148−149*, 258−268.

(30) Wang, F.; Li, W.; Gu, S.; Li, H.; Ren, C.; Liu, X. Construction of Eu₂O₃/g-C₃N₄ Redox Heterojunctions Containing Eu³⁺/Eu²⁺ Self-Redox Centers for Boosted Visible-Light Photocatalytic Activity. *Eur. J. Inorg. Chem.* **2018**, *2018* (22), 2564−2573.

(31) Marzouki, R.; Abd-Rabboh, H. S. M.; Baker, A. H.; Ghazwani, S. A.; Zid, M. F.; Hamdy, M. S. Synthesis, Characterisation and the Photocatalytic Performance of Europium Oxide/Ceria Nanocomposite. *Int. J. Environ. Anal. Chem.* **2021**, *101* (15), 2539−2550.

(32) Hernández-Carrillo, M. A.; Torres-Ricárdez, R.; García-Mendoza, M. F.; Ramírez-Morales, E.; Rojas-Blanco, L.; Díaz-Flores, L. L.; Sepúlveda-Palacios, G. E.; Paraguay-Delgado, F.; Pérez-Hernández, G. Eu-Modified ZnO Nanoparticles for Applications in Photocatalysis. *Catal. Today* **2020**, *349*, 191−197.

(33) Wei, D.; Huang, Y.; Bai, J.; Seo, H. J. Manipulating Luminescence and Photocatalytic Activities of BiVO₄ by Eu3⁺ Ions Incorporation. *J. Phys. Chem. C* **2020**, *124* (22), 11767−11779.

(34) Du, F.; Yang, D.; Sun, Y.; Jiao, Y.; Teng, F.; Fan, H. Electrospun Zn-Doped Ga₂O₃ Nanofibers and Their Application in Photodegrading Rhodamine B Dye. *Ceram. Int.* **2021**, *47* (4), 4963−4971.

(35) Li, L.; Xu, K.; Wang, Y.; Hu, Z.; Zhao, H. Enhanced Persistent Luminescence and Photocatalytic Properties of Ga_2O_3:Cr^{3+} by In^{3+} Doping. *Opt. Mater. Express* **2016**, *6* (4), 1122−1130.

(36) Babu, B.; Kadam, A. N.; Rao, G. T.; Lee, S.-W.; Byon, C.; Shim, J. Enhancement of Visible-Light-Driven Photoresponse of Mn-Doped SnO_2 Quantum Dots Obtained by Rapid and Energy Efficient Synthesis. *J. Lumin.* **2018**, *195*, 283−289.

(37) Godymchuk, A.; Papina, I.; Karepina, E.; Kuznetsov, D.; Lapin, I.; Svetlichnyi, V. Agglomeration of Iron Oxide Nanoparticles: pH Effect Is Stronger than Amino Acid Acidity. *J. Nanopart. Res.* **2019**, *21* (10), 208.

(38) Dong, Q.; Tian, Z.; Song, W.; Deng, W.; Zhang, H. Catalytic Oxidation of Lignin and Model Compounds over Nano Europium Oxide. *Colloids Surf., A* **2021**, *626*, 126846.

(39) Cho, E.-J.; Oh, S.-J. Surface Valence Transition in Trivalent Eu Insulating Compounds Observed by Photoelectron Spectroscopy. *Phys. Rev. B: Condens. Matter Mater. Phys.* **1999**, *59* (24), R15613−R15616.

(40) Zhang, P.; Zhao, Y.; Zhai, T.; Lu, X.; Liu, Z.; Xiao, F.; Liu, P.; Tong, Y. Preparation and Magnetic Properties of Polycrystalline Eu_2O_3 Microwires. *J. Electrochem. Soc.* **2012**, *159* (4), D204−D207.

(41) Ren, C.; Li, W.; Li, H.; Liu, X.; Liu, Y.; Li, X.; Lin, C.; Zhou, H. Ultrasmall Pt Nanoclusters Deposited on Europium Oxide: A Newly Active Photocatalyst for Visible-Light-Driven Photocatalytic Hydrogen Evolution. *Appl. Surf. Sci.* **2019**, *480*, 96−104.

(42) Li, C.; Xu, L.; Zhao, Y.; Sun, J.; He, D.; Jiao, H. Synthesis, Morphology, Photoluminescence and Photocatalytic Properties of Yolk-Shell Au@Y_2O_3:Eu^{3+} Sub-Microspheres. *J. Alloys Compd.* **2015**, *627*, 31−38.

(43) Xie, Y.; Wu, J.; Sun, C.; Ling, Y.; Li, S.; Li, X.; Zhao, J.; Yang, K. La_2O_3-Modified Graphite Carbon Nitride Achieving the Enhanced Photocatalytic Degradation of Different Organic Pollutants under Visible Light Irradiation. *Mater. Chem. Phys.* **2020**, *246*, 122846.

(44) Wang, B.-Y.; Li, E.-D.; Zong, Y.-C.; Wang, X.-B.; Yuan, J.; Zhang, F.-Q. Fabricating Hollow, Multishell CeO_2 Microspheres for Enhanced Photocatalytic Degradation of RhB under Visible Light. *J. Mater. Res.* **2022**, *37* (5), 1070−1082.

(45) Qi, Y.; Ye, J.; Zhang, S.; Tian, Q.; Xu, N.; Tian, P.; Ning, G. Controllable Synthesis of Transition Metal Ion-Doped CeO_2 Micro/Nanostructures for Improving Photocatalytic Performance. *J. Alloys Compd.* **2019**, *782*, 780−788.

(46) Niu, T.; Zhang, P.; Zheng, G.; Liu, L.; Deng, J.; Jin, Y.; Jiao, Z.; Sun, X. Tuning the Charge Transition Process of Eu_2O_3 Nanorods by Coupling with Ag Nanoparticles for Enhanced Photocatalytic Performance. *J. Environ. Chem. Eng.* **2017**, *5* (3), 2930−2936.

(47) Wang, Y.; Qian, B.; Zhao, Q.; Duan, T.; Xie, F.; Zou, H.; Song, Y.; Zhou, X.; Sheng, Y. Controllable Synthesis of Bifunctional Material $Ca_2Ti_2O_6$:Eu^{3+} and Its Comparative Study on Luminescence and Photocatalytic Properties with $CaTiO_3$:Eu^{3+}. *Ceram. Int.* **2022**, *48* (12), 17157−17170.